

# A Light-Driven Microgel Rotor

Hang Zhang, Lyndon Koens, Eric Lauga, Ahmed Mourran,\* and Martin Möller

The current understanding of motility through body shape deformation of micro-organisms and the knowledge of fluid flows at the microscale provides ample examples for mimicry and design of soft microrobots. In this work, a 2D spiral is presented that is capable of rotating by non-reciprocal curling deformations. The body of the microswimmer is a ribbon consisting of a thermoresponsive hydrogel bilayer with embedded plasmonic gold nanorods. Such a system allows fast local photothermal heating and nonreciprocal bending deformation of the hydrogel bilayer under nonequilibrium conditions. It is shown that the spiral acts as a spring capable of large deformations thanks to its low stiffness, which is tunable by the swelling degree of the hydrogel and the temperature. Tethering the ribbon to a freely rotating microsphere enables rotational motion of the spiral by stroboscopic irradiation. The efficiency of the rotor is estimated using resistive force theory for Stokes flow. This research demonstrates microscopic locomotion by the shape change of a spiral and may find applications in the field of microfluidics, or soft microrobotics.

developed swimming strategies that do not apply to the macroscopic world due to the high viscous drag experienced by the body at a length scale where the inertial forces are negligible.<sup>[5,6]</sup> The ratio between these forces defines the Reynolds number  $Re$ , which is on the order of  $10^{-4}$  for micro-organisms.<sup>[5]</sup> Two major mechanisms used by micro-organism to swim and stir surrounding fluids are the beating of the cilia and rotating of the helical flagella, which are filaments capable of active bending deformation or rotation.<sup>[5–10]</sup> These filaments driven by internally generated forces work with viscous and elastic forces to generate propulsive thrusts.<sup>[11–13]</sup> The physical balance between elastic forces and viscous drag determines the swimming speed, or pumping frequency and performance.<sup>[14]</sup>

## 1. Introduction


Micro-organisms are ubiquitous in our world and their locomotion in the form of swimming is an essential part of their lives. Prokaryotes (e.g., the model bacterium *Escherichia coli*) and eukaryotes (e.g., *Paramecium* and alga *Chlamydomonas*) swim to explore their chemical environment,<sup>[1,2]</sup> pursue food,<sup>[3]</sup> or escape predation.<sup>[4]</sup> Similarly, spermatozoa swim using flagella to spread progeny. Being small, micro-organisms have

To our best knowledge, a microswimmer based on curling of a 2D spiral is yet to be found in nature, though helical-shaped micro-organisms are abundant, such as *spirilla* and spirochetes. Curling is a way to store elastic energy and is widely used in engineering, such as piezoelectric devices,<sup>[15]</sup> energy storage in clock springs, or 3D displacement in artificial muscles.<sup>[16]</sup> In this report, we present a novel type of microswimmer, i.e., a spiral-shaped microgel that is capable of rotating by nonreciprocal deformations. The body of the microswimmer is ribbon-shaped and consists of a cross-linked poly(*N*-isopropylacrylamide) (PNIPAM) hydrogel laden with gold nanorods (AuNRs). AuNRs are engineered to absorb photon energy in the near infrared and generate localized heat that triggers volume changes of the surrounding hydrogel.<sup>[17–19]</sup> Coated on one surface with a thin metal layer, the bilayer hydrogel ribbon is able to swell and curl in water along its length to form a 2D spiral.<sup>[20–22]</sup> Upon heating, the solubility decrease of the polymer network causes the hydrogel layer to shrink, so that the spiral unwinds. We note here that the bending rigidity of the ribbon and its stiffness are greatly affected by the water content in it. The light-induced temperature-jumps give rise to mechanical response over a few hundred milliseconds, where the rate-limiting factor is the mass transport within the gel.<sup>[22–28]</sup> We hypothesize that photothermal heating creates a transient state, where an imbalance exists between the stresses defining the local and the mean curvature of the ribbon.<sup>[21]</sup> These elastic restoring forces of bending and stretching are counterbalanced by the viscous drag of the surrounding fluid, which sets the rotor in motion. Since the material is relatively soft, the curling dynamics depends strongly on the dissipation mechanisms.<sup>[21,29,30]</sup>

Unlike previous studies that focused on the end equilibrium states of the hydrogel volume-phase transition, we study the response dynamics upon short-lived stimuli here, an aspect that

Dr. H. Zhang,<sup>[†]</sup> Dr. A. Mourran, Prof. M. Möller  
DWI Leibniz-Institute for Interactive Materials  
RWTH Aachen University  
Forckenbeckstr. 50, D-52056 Aachen, Germany  
E-mail: mourran@dwil.rwth-aachen.de

Dr. L. Koens  
Department of Mathematics and Statistics  
Macquarie University  
192 Balaclava Rd, Macquarie Park, NSW 2113, Australia  
Prof. E. Lauga  
Department of Applied Mathematics and Theoretical Physics  
University of Cambridge  
Wilberforce Road, Cambridge CB3 0WA, UK

 The ORCID identification number(s) for the author(s) of this article can be found under <https://doi.org/10.1002/sml.201903379>.

© 2019 The Authors. Published by WILEY-VCH Verlag GmbH & Co. KGaA, Weinheim. This is an open access article under the terms of the Creative Commons Attribution License, which permits use, distribution and reproduction in any medium, provided the original work is properly cited.  
The copyright line for this article was changed on 15 October 2019 after original online publication.

<sup>[†]</sup>Present address: Department of Applied Physics, Aalto University, Puumiehenukka 2, 02150 Espoo, Finland

DOI: 10.1002/sml.201903379

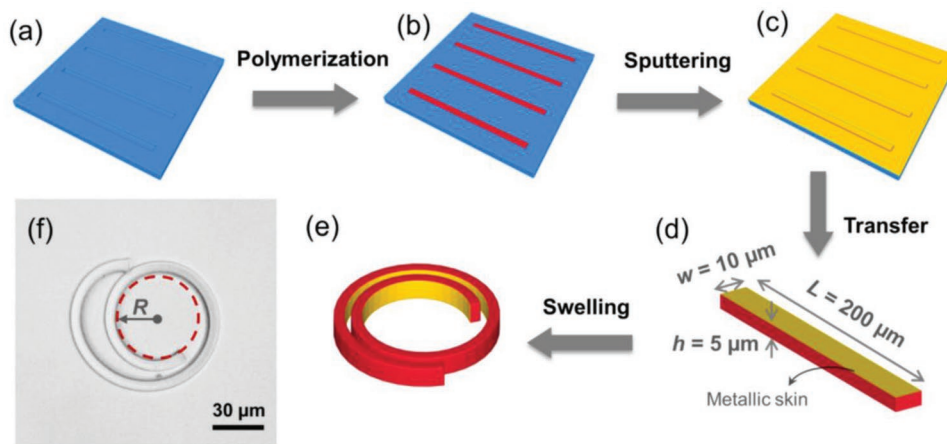


**Figure 1.** Fabrication of bilayer spiral microgels. a–e) Schematic illustration of the fabrication of the hydrogel bilayer. a) Perfluoropolyether (PFPE) mold replicated from a silicon master. b) Microgels polymerized inside the mold. c) Sputter-coating of a thin metallic skin on the microgel. d) Dimension of the as-prepared microgel particle. e) Microgel bilayer after swelling. f) Optical microscopy image of a spiral microgel at 20 °C. Inner radius  $R$  is indicated by the dashed circle.

is less well-understood.<sup>[27,28,31]</sup> We show that the light-driven microgel undergoes time-dependent deformations and provides mechanical work. The light energy in the near-infrared causes the gel's shape to change outside thermodynamic equilibrium, and it is possible to probe the kinematics of the deformation by the frequency of the light's strobe.<sup>[17]</sup> The material is shaped by the swelling of the gel, reminiscent to the hydraulic force that erects the butterfly proboscis or that coils tendrils plants,<sup>[32,33]</sup> raising questions about the differences and similarity of the synthetic ribbon to those biological counterparts. In the following, the fabrication and light-driven motion of the spiral microrotor are demonstrated. Through quasi-static heating, we assessed the changes in curvature as a function of the misfit strain. A measure of the maximum speed would require linking the bending wave and stiffness of the microgel ribbon with respect to the frequency of cyclic irradiation,<sup>[7]</sup> an issue not addressed here but will be pursued in the near future. Finally, the efficiency of the system is estimated based on the resistive force theory.

## 2. Results and Discussion

### 2.1. Thermoresponsive Property of a 2D Spiral

The fabrication of the 2D spiral microgel is illustrated schematically in **Figure 1a–e** along with an optical microscopy image showing the resultant spiral microgel in water at 20 °C. Details of the process can be found in the experimental section. Briefly, a nonwetting soft mold is replicated from a silicon master (Figure S1, Supporting Information) made by photolithography with desired dimensions. Isolated microgel particles containing AuNRs can be then molded inside the soft template by photopolymerization with highly defined shape and composition.<sup>[20,34]</sup> After polymerization, the top surfaces of the microgels are sputter-coated by a gold skin layer, after which the microgels are released into water by a transfer process. Upon swelling in water, the expansion of the gel layer is restricted by the gold skin, which resists stretching. It is therefore a bilayer ribbon in which

one layer expands more relative to the other upon actuation.<sup>[35]</sup> Consequently, swelling of the hydrogel causes differential strain that leads to bending of the bilayer. Depending on the initial geometry of the ribbon, different structures can be formed such as a helix or 2D spiral.<sup>[20]</sup> In this report, we focus on the ribbon with an as-prepared size of  $5 \mu\text{m} \times 10 \mu\text{m} \times 200 \mu\text{m}$ , which bends and forms a 2D spiral upon swelling in water.

The thermoresponse of the microgel bilayer was investigated by measuring the change of the curvature at different temperatures. **Figure 2** shows that as the temperature approaches the volume phase transition temperature of the PNIPAM network, the spiral unbends and nearly recovers its original straight shape. The diagram in **Figure 2b** shows the straightening of the spiral with temperature, which increases the radius and decreases the length of the ribbon due to the de-swelling of the gel layer. This property can be understood by examining the dependence of the curvature on the relative strain normalized to the thickness, i.e.,  $\epsilon/h$ , where  $\epsilon = L - L_0$  ( $L_0 = 200 \mu\text{m}$ ) represents the relative variation in the ribbon length and  $h$  is the thickness (see **Figure 2c**). The dependence is rather linear, which is reminiscent of Timoshenko's bending bimetallic strip.<sup>[36]</sup> In that case the curvature is proportional to the misfit strain between the two layers and inversely proportional to the thickness of the strip. It is also worth noting that the slope is close to that of a helical microgel with a similar aspect ratio,<sup>[20]</sup> which emphasizes the role of geometry and hydrogel composition in defining the mechanical response of the hydrogel bilayer. The dramatic change of the curvature, especially near the volume phase transition temperature, is an important feature of the bilayer system that can be utilized to perform mechanical work at the expense of a small change in the volume.

### 2.2. Nonreciprocal Actuation via Photothermal Heating

To fabricate the microgel rotor, a silica microsphere (diameter  $\approx 10 \mu\text{m}$ ) was attached to one end of the microgel as shown in the optical microscopy image of **Figure 3c**. This was done

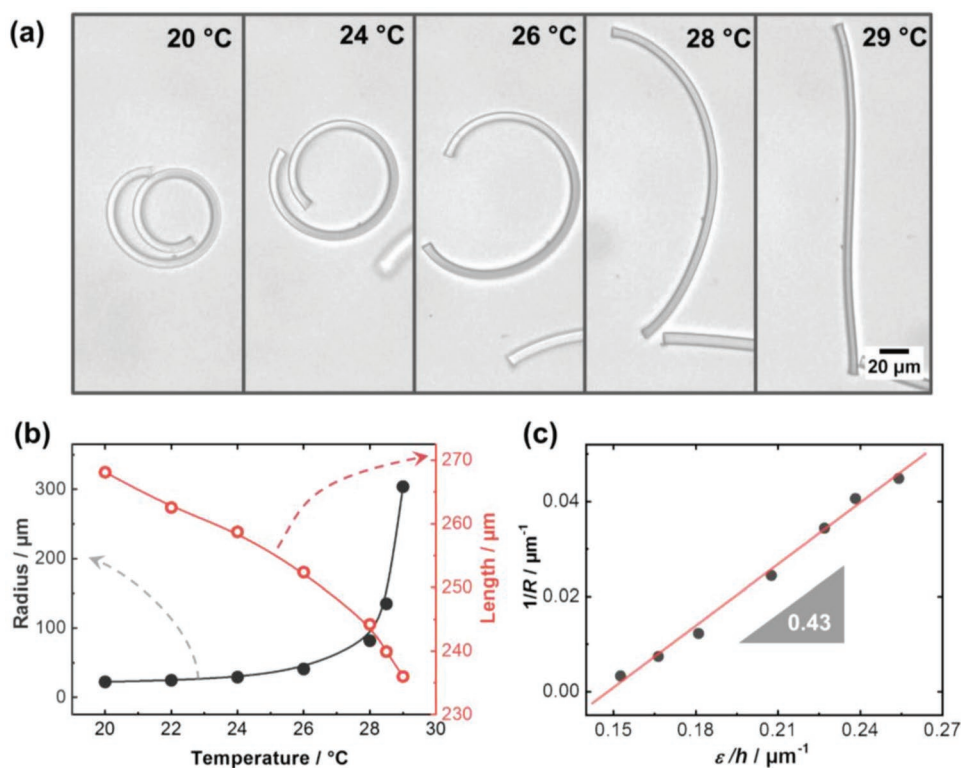


**Figure 2.** Characterization of the spiral microgel at different temperatures. a) Optical images of the spiral at different temperatures. b) The change of the spiral length and the radius with temperature. c) Curvature ( $1/R$ ) of the spiral versus strain  $\epsilon$  relative to the ribbon thickness  $h$ .

by incubating the spiral microgels with silica particles for 5 min under stroboscopic irradiation to facilitate the adsorption. To minimize bundling of the microgels or adsorption of several spheres per spiral, the colloidal solution was diluted to  $0.0005 \text{ mg mL}^{-1}$  and the spirals were fairly separated from each other, so that we could find and use the one that had only one microsphere attached at the end. The adhesion between the microspheres and the spiral microgel is partially due to hydrophobic interactions,<sup>[37]</sup> presumably because the silica microparticles were not fully hydrophilic. Besides, it has been shown that nanoparticle adsorb onto polymer gels and act as connectors between polymer chains, providing the ability for polymer chains to reorganize and dissipate energy under stress.<sup>[38]</sup> The adhesion was rather strong, as no desorption was observed throughout our experiments, even when the spiral undergoes a translation (Video S1, Supporting Information). The spiral was then confined edge-on between two glass surfaces such that the microsphere can freely rotate without significant lateral displacement (Figures S2 and S3, Supporting Information). This was made possible by driving the freely moving microgel ribbon into the center area of the confinement, where the distance approaches  $10 \text{ }\mu\text{m}$  (Video S1, Supporting Information). Upon stroboscopic irradiation at 808 nm, close to the longitudinal surface plasmon resonance of the AuNRs that have an absorption maximum around 791 nm,<sup>[20]</sup> the spiral underwent photothermally induced bending/unbending deformations as demonstrated in Figure 3a and Videos S2–S5 (Supporting Information). By comparing the unwound shape of the spiral microgel under irradiation and the microgel under external heating in equilibrium state, the local

temperature of the hydrogel under irradiation can be estimated to be at least  $29 \text{ }^\circ\text{C}$ , consistent with our previous work.<sup>[17]</sup> On the other hand, no significant temperature gradient is expected inside the gel, since the heat is mainly produced on AuNRs uniformly distributed inside the hydrogel ( $9 \text{ AuNRs }\mu\text{m}^{-3}$ )<sup>[20]</sup> and the light attenuation at 808 nm is relatively weak across the thickness of the hydrogel (optical density  $\approx 0.12$ ).

Figure 3a shows the shape-superimposition during an actuation cycle, i.e., irradiation for 500 ms and recovery (light off) for 500 ms. The period was chosen based on the characteristic time for the water to diffuse in and out of the microgel with a thickness of  $5 \text{ }\mu\text{m}$ , which is in the range from sub-second to a few seconds.<sup>[17,39,40]</sup> The spiral continuously unfurls to an almost straight shape within 0.5 s of irradiation as seen in the optical microscopy images, and rewinds during the recovery stroke (0.5 s off). At the end of each irradiation cycle, the microgel recovers its spiral shape with an anticlockwise rotation with respect to the initial position. The Reynolds number of the spiral microgel can be estimated to be around  $10^{-2}$  using the width of the microgel as the characteristic length ( $10 \text{ }\mu\text{m}$ ) and a typical velocity of  $1000 \text{ }\mu\text{m s}^{-1}$ , which is estimated from the velocity of the end of the spiral. The rotation of the spiral can be clearly observed after a few cycles as shown by the superimposed images taken at the beginning of each cycle in Figure 3b. The spiral exhibited a net anticlockwise rotation around the microsphere with an average speed of  $22^\circ$  per cycle.

As shown in previous works, one necessary condition to obtain swimming at low Reynolds numbers is that the deformation path during one cycle should follow different paths in the

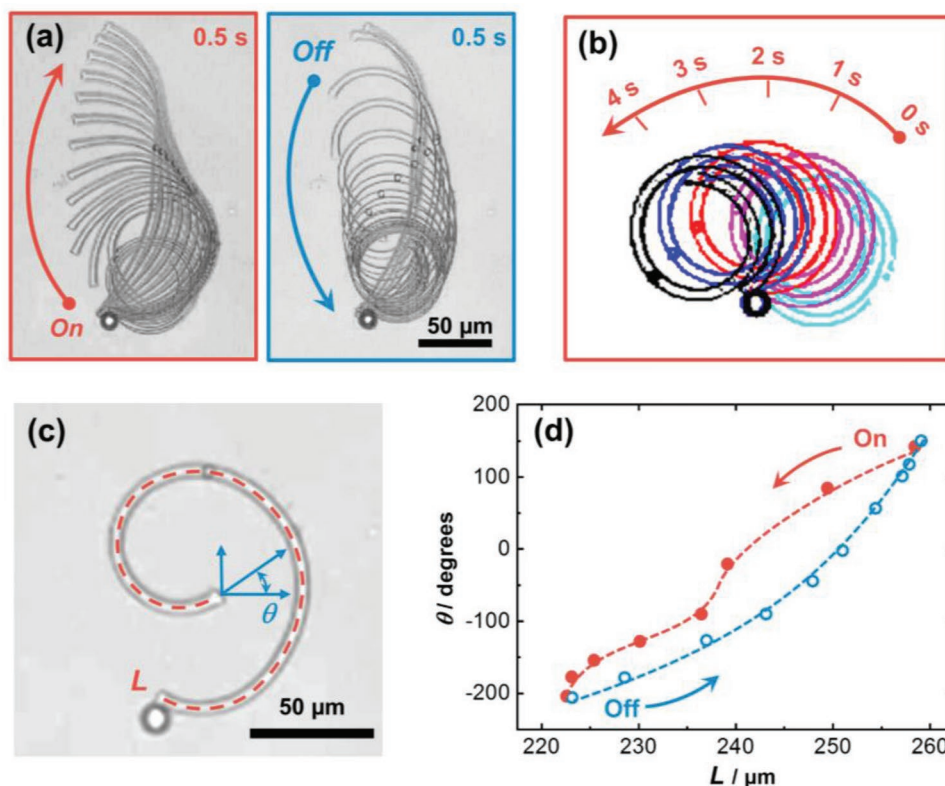


**Figure 3.** Photothermal actuation of a spiral rotor tethered to a freely rotating sphere. a) Superimposed optical microscopy images of the spiral rotor under stroboscopic irradiation. Left: on-time (0.5 s); right: off-time (0.5 s). Laser intensity:  $1.7 \text{ W mm}^{-2}$  at 808 nm. b) Superimposition of the thresholded outline of the spiral rotor under stroboscopic irradiation (0.5–0.5 s). From right to left: at 0, 1, 2, 3, and 4 s. c) Optical microscopy image of the spiral rotor during recovery. The length of the centerline ( $L$ , red-dashed line) and the tangential angle ( $\theta$ ) are marked correspondingly. d) Change of the  $L$  versus  $\theta$  during one cycle of irradiation (0.5–0.5 s). Arrows mark the direction of change, and dashed lines are drawn to guide the eye.

shape space.<sup>[5–7,41]</sup> Indeed, it can be observed from the superimposition in Figure 3a that the deformation sequence during the recovery stroke is different from the power stroke, and the evolution of curvature differs as well. The kinematics of the spiral shows a close resemblance to the cilia in eukaryotic cells as demonstrated in the literature.<sup>[42]</sup> The power stroke of a real cilium is characterized by the almost rigid rotation around its base, while the recovery stroke shows a large curvature to produce the nonreciprocal deformations, i.e., the nonidentical sequence of shapes during one cycle under a time-reversal symmetry. Two geometric parameters were selected to characterize the deformation: the length of the center line ( $L$ ) and the tangential angle ( $\theta$ ) of the free end as illustrated in Figure 3c, see Figure S4 (Supporting Information) for the image analysis.<sup>[43]</sup> The evolution of these two parameters is plotted in Figure 3d with the  $L$  as  $X$ -axis and  $\theta$  as  $Y$ -axis, demonstrating the time-independent deformation during one cycle. Unbending of the spiral structure under laser irradiation resulted in a decrease of the length from 258 to 222  $\mu\text{m}$  and a decrease of  $\theta$  from  $142^\circ$  to  $-203^\circ$ . The continuous decrease in  $L$  is due to the shrinking of the gel, while the change in the  $\theta$  indicates the local deformation of the spiral. The microgel contour length at the end of the irradiation is close to the length at  $29^\circ\text{C}$  (as indicated in Figure 2b). In contrast, the recovery stroke (off-time) follows a distinct path different to that of the power-stroke. The steady increase in the length during the off-time is due to the swelling of the hydrogel

layer upon cooling. Meanwhile, the winding of the spiral results in the continuous increase of  $\theta$  to more than  $150^\circ$ . This value is slightly larger than the starting point in the cycle due to the net rotation of the spiral after one cycle of actuation. The non-reciprocal deformation can be attributed to the combination of nonequilibrium actuation and bending of the bilayer.<sup>[17]</sup>

Figure 4 shows the influence of irradiation period on the spiral net rotation. For a short irradiation period of 0.1–0.1 s, the spiral microgel is not able to wind back due to the short recovery time. The actuation amplitude, defined as the displacement of the free end before and after irradiation, is rather small in this case. Nevertheless, the asymmetry of the motion kinematics during an irradiation cycle is still distinguishable in Figure 4a with a net rotational motion of  $1.6^\circ \text{ s}^{-1}$  (see Figure 4d). Longer irradiation periods increase the motion amplitude and enhance the asymmetry in the motion kinematics as shown in Figure 4b,c. Figure 4b shows a significantly larger amplitude as well as asymmetric kinematics compared to Figure 4a with an increased rotational speed, i.e.,  $16.7^\circ \text{ s}^{-1}$ . The longest irradiation period is 2 s in Figure 4c. Note that at the end of the irradiation, the ribbon is slightly bent in the opposite direction. This can be attributed to the shrinkage of the hydrogel causing the bilayer to bend in the opposite direction.<sup>[20]</sup> The angular velocity in this case is  $8.8^\circ \text{ s}^{-1}$ . In Figure 4d, the angular velocity of rotation shows a maximum of  $22^\circ \text{ s}^{-1}$  at the  $t_{\text{on}}$  of 0.5 s. This is in an interesting correlation

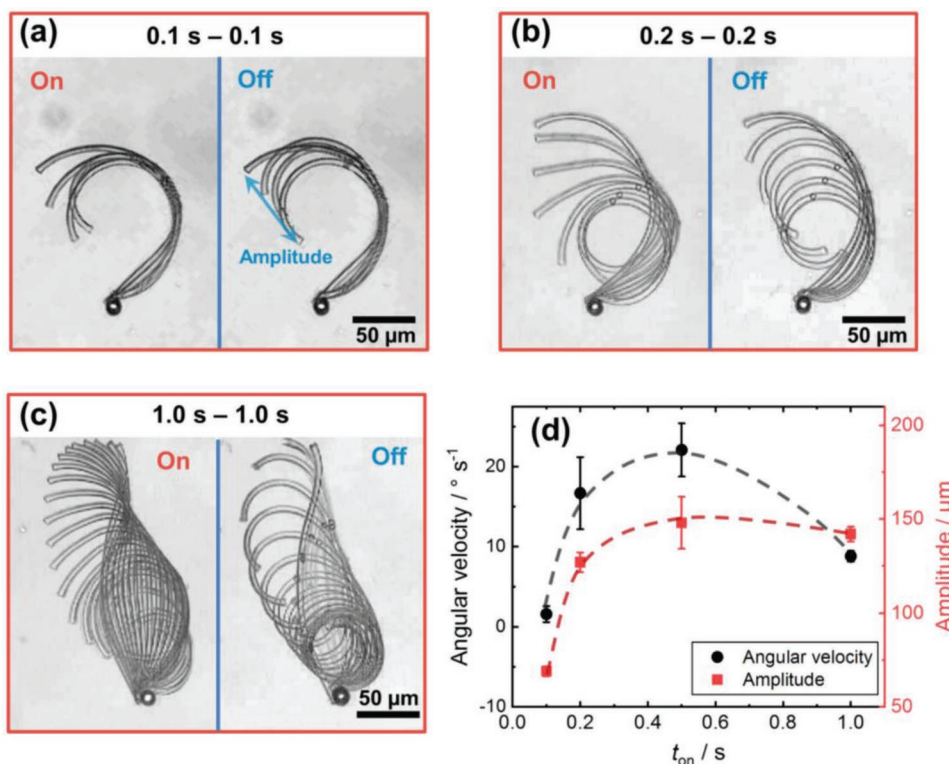


**Figure 4.** Spiral rotor at different modulation frequency. a–c) Superimposed optical microscopy images of the spiral under different stroboscopic irradiation. On–off irradiation time from (a) to (c): 0.1–0.1s, 0.2–0.2 s, and 1.0–1.0 s. Scale bar: 50 μm. Laser intensity: 1.7 W mm<sup>-2</sup> at 808 nm. The amplitude of actuation is marked in (a). d) Dependency of angular velocity on the duration of on-time  $t_{on}$ . Each data point is averaged from five cycles of irradiation, and the error bar shows the standard deviation. Dashed lines are drawn to guide the eyes.

with the amplitude of actuation, where the largest amplitude appears also at  $t_{on}$  of 0.5 s. At this irradiation period, the spiral microgel already reached a fully stretched state, so that the amplitude did not further increase upon longer irradiation. At the  $t_{on}$  of 1.0 s, the rotation per cycle is close to the  $t_{on}$  of 0.5 s, which resulted in a decrease of the angular velocity, calculated from the  $\frac{\text{Rotation per cycle}}{\text{Period}}$ . In this context, we also note that a longer irradiation time ( $t_{on} = 1$  s) induces an inversion of the ribbon curvature at the end of irradiation (Figure 4c), similar to what we have shown previously.<sup>[20]</sup> This may also cause a slight backward motion that limits the rotation per cycle.

### 2.3. Theoretical Estimation of Power and Efficiency

The efficiency of the deforming spiral rotor is determined by the ratio of the power required to rotate the body compared to the input power, therefore a perfectly efficient rotor would have an efficiency close to 1. At microscopic scales, the drag from the fluid on the body is linearly related to the object's linear and angular velocity. As such the torque on the fluid and the power dissipation from the rotation can be written as

$$\tau = R_{\tau} \Omega \quad (1)$$

$$P = \tau \Omega = R_{\tau} \Omega^2 \quad (2)$$

where  $\tau$  is the torque on the fluid,  $\Omega$  is the angular velocity,  $P$  is the power, and  $R_{\tau}$  is a linearity coefficient that depends on the geometry of the shape. For long thin objects in Stokes flow,  $R_{\tau}$  can be estimated with a technique called resistive force theory.<sup>[44]</sup> This theory relates the force per unit length along the elongated body,  $\mathbf{f}$ , to the velocity of the filament at that location,  $\mathbf{U}$ , through the equation

$$\mathbf{f} = -[\zeta_t \hat{\mathbf{t}}\hat{\mathbf{t}} + \zeta_n (I - \hat{\mathbf{t}}\hat{\mathbf{t}})] \cdot \mathbf{U} \quad (3)$$

where  $I$  is the identity matrix,  $\hat{\mathbf{t}}$  is the tangent vector to the centreline of the filament and  $\zeta_t$  and  $\zeta_n$  are drag coefficients for motion tangent and perpendicular to the centerline, respectively. This relationship is shown diagrammatically in Figure 5.

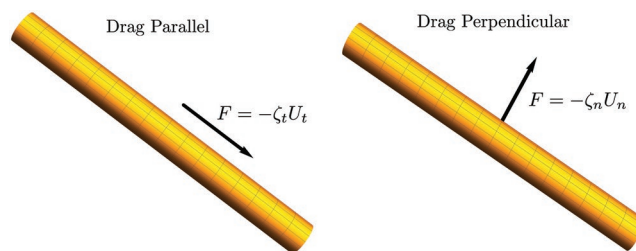


**Figure 5.** Diagrammatic illustration of the drag parallel and perpendicular to the filament.

These drag coefficients increase significantly when very close to walls. In this limit the flow is known as the lubrication flow and is governed by steep gradients in the velocity. In this lubrication limit the drag per unit length on a cylinder, from a single wall, moving normal to the axis is given by<sup>[45]</sup>

$$\zeta_{n,1\text{wall}} = \frac{2\pi\mu\sqrt{2r_b}}{\sqrt{\epsilon}} \quad (4)$$

where  $\mu$  is the viscosity of the fluid,  $r_b$  is the radius of the filament and  $\epsilon$  is the separation between the particle and the wall. Since the spiral rotor is closely confined between two walls, and lubrication forces are additive, the normal drag coefficient is found by adding the contribution from both walls. Hence, assuming that the body is equidistant from the walls the drag for motion perpendicular to the centerline can be written as

$$\zeta_n = \frac{8\pi\mu\sqrt{r_b}}{\sqrt{h-2r_b}} \quad (5)$$

where  $h$  is the separation between the two walls. Though the normal motion of the rotor is governed by lubrication forces, tangential motions do not induce lubrication. The tangential drag on these systems therefore depends on the full geometry near the walls. Conveniently in the limit  $r_b \ll h/2 \ll L$ , where  $L$  is the arclength, the tangential drag on a cylinder between two walls has been shown to be<sup>[43]</sup>

$$\zeta_t = \frac{2\pi\mu}{\log(h/r_b) - 0.453} \quad (6)$$

Formally this coefficient does not apply to the gel swimmer as  $r_b \sim h/2$ . However, as lubrication forces are typically much larger, it is a suitable approximation.

In the resistive force theory formulation  $R_\tau$  is found by determining the torque on the fluid generated from a unit angular velocity perpendicular to the planes,  $\hat{\mathbf{z}}$ . Mathematically this means evaluating

$$R_\tau = - \int ds \mathbf{r}(s) \times \left[ \left[ \zeta_n \hat{\mathbf{t}}(s) \hat{\mathbf{t}}(s) + \zeta_t (\mathbf{I} - \hat{\mathbf{t}}(s) \hat{\mathbf{t}}(s)) \right] \cdot (\hat{\mathbf{z}} \times \mathbf{r}(s)) \right] \quad (7)$$

where  $\mathbf{r}(s)$  is the equation for centerline of the slender-body centered around the attachment point and  $s$  is the arclength. The power dissipation by fluid motion can therefore be estimated using this formula if a suitable approximation of the shape is available.

Since the spiral rotor periodically changes between a wound loop and a straight rod, we will estimate the viscous power dissipation for both a rotating loop and rotating straight rod. The centerline description for each of these cases is

$$r_{\text{rod}}(s) = \{s, 0, 0\} \quad (8)$$

$$r_{\text{loop}}(s) = R \left\{ \sin\left(\frac{2\pi s}{L}\right), 1 - \cos\left(\frac{2\pi s}{L}\right), 0 \right\} \quad (9)$$

where  $s$  goes from 0 to  $L$ ,  $R$  is the radius of the loop and we have written the parameterization in the Cartesian coordinates  $\{x, y, z\}$ . For these shapes the linearity coefficients become

$$R_\tau^{\text{loop}} = -\pi R^3 (\zeta_n + 3\zeta_t) \quad (10)$$

$$R_\tau^{\text{rod}} = -\zeta_n \frac{L^3}{3} \quad (11)$$

These values correspond to power outputs of

$$P_{\text{loop}} \approx -3.75 - 12.3 \times 10^{-16} \text{ Js}^{-1} \quad (12)$$

$$P_{\text{rod}} \approx -1.6 - 6.9 \times 10^{-14} \text{ Js}^{-1} \quad (13)$$

where we have used  $R = 25 \mu\text{m}$ ,  $\Omega = 0.385 \text{ radians s}^{-1}$ ,  $\mu = 10^{-3} \text{ Pa s}$ ,  $h = 10 \mu\text{m}$ ,  $L = 240 \mu\text{m}$ , and  $r_b = 3.2\text{--}4.85 \mu\text{m}$ .

The irradiation energy exerted on the microgel can be estimated from the exposure intensity ( $1.7 \text{ W mm}^{-2}$ ) and the surface area of the microgel. By assuming the incident angle is  $90^\circ$ , the surface area of the microgel that receives irradiation is roughly  $1000 \mu\text{m}^2$ . The average input power is therefore  $1.7 \times 10^{-3} \text{ J s}^{-1}$ . The efficiency can thus be calculated to be on the order of  $10^{-12}\text{--}10^{-13}$  for loops and  $10^{-11}\text{--}10^{-12}$  for rods. To put this in context, the efficiency of other light powered microscopic devices have been estimated between  $10^{-8}$  and  $10^{-10}$  for thermocapillary devices,<sup>[46]</sup>  $10^{-11}$  for bacterial devices,<sup>[47]</sup> and  $10^{-15}$  for direct momentum transfer.<sup>[46]</sup> The efficiency obtained herein is therefore much higher than direct momentum transfer techniques and is of a similar magnitude to other light powered systems.

Furthermore, this efficiency can be thought of as a lower bound for the following reasons. 1) The relatively low absorbance ( $\approx 0.12$  in the thickness direction) of the microgel object due to small dimension, which means roughly 75% of incident light energy is transmitted through the hydrogel object and lost. 2) Large heat capacity of the gel that requires a significant portion of the energy to be consumed in order to heat the microgel object ( $\approx 6 \times 10^{-7} \text{ J}$  in 4 s, see the Supporting Information). 3) Constant heat dissipation due to temperature difference between the microgel and surrounding water. Therefore, the efficiency can be improved if the above aspects are taken into consideration, such as further increasing the concentration of AuNRs, and choosing a polymer matrix with a lower volume phase transition temperature so that less energy is required to trigger the deformation.

### 3. Conclusion

We have engineered a micrometer-scale hydrogel bilayer ribbon that curls upon swelling in water, resulting in a spiral with tunable mechanical responses. The photoinduced heating of the gold nanorods embedded in the microgel ensures a rapid and precise change in temperature within the object and can be utilized to control the swelling state of the PNIPAM network. The resulting expansion/shrinkage of the hydrogel causes the winding and unwinding of the spiral. Energy-transducing nanorods combined with the thermal dissipation capacity of water enables the microgel's shape to change out of the thermodynamic equilibrium, as the thermal diffusion processes

(heating/cooling) are up to 100 times faster than the mass diffusion processes (volume change). Light as an energy feed is particularly relevant because the frequency of strobe irradiation now dictates the kinematics of curling deformation and allows nonreciprocal bending and unbending cycles that follow distinct paths, which are required for a net rotational thrust at low  $Re$ . Using a resistive force formalism, the efficiency of the current system was estimated to be about  $10^{-12}$  and is comparable with other light driven systems. Furthermore, we have proposed additional experimental considerations in order to improve the efficiency of our system for future investigations.

This study opens the new avenue for artificial microswimmers that can be remotely actuated by a near-infrared laser with temporal resolution down to milliseconds and spatial responsiveness in the micrometer range. This design principle may also be extended to program other motile elements, in order to be utilized for biomedical and microfluidic applications, as well as for the development of novel soft microrobotics.

#### 4. Experimental Section

**Synthesis of Gold Nanorods:** AuNRs were synthesized via a modified seed-mediated method.<sup>[48]</sup> All chemicals were purchased from Sigma-Aldrich unless otherwise mentioned, and deionized water ( $0.1 \mu\text{S cm}^{-1}$ , ELGA Purelab-Plus) was used throughout the experiments. To make the seeds, freshly prepared ice-cold  $\text{NaBH}_4$  (99%)  $0.010 \text{ M}$  aqueous solution ( $0.60 \text{ mL}$ ) was quickly injected to a mixture of water ( $4.2 \text{ mL}$ ),  $0.20 \text{ M}$  Cetyltrimethylammonium bromide (CTAB, 99%,  $5.0 \text{ mL}$ ) and  $0.0030 \text{ M}$  hydrogen tetrachloroauric(III) acid ( $\text{HAuCl}_4$ , 99.9%,  $0.83 \text{ mL}$ ) under vigorous stirring, and the seed solution was further stirred for 10 min. For the growth solution,  $0.20 \text{ M}$  CTAB ( $150 \text{ mL}$ ),  $0.050 \text{ M}$  ascorbic acid (99%,  $3.1 \text{ mL}$ ), and  $0.0080 \text{ M}$   $\text{AgNO}_3$  (99.99%,  $3.3 \text{ mL}$ ) were added to  $0.0010 \text{ M}$   $\text{HAuCl}_4$  ( $150 \text{ mL}$ ) under stirring. The temperature of growth solution was kept at  $25^\circ\text{C}$  in water bath. The seed solution ( $0.875 \text{ mL}$ ) was injected into the growth solution under vigorous stirring for 30 min. Afterward  $0.050 \text{ M}$  ascorbic acid ( $2.0 \text{ mL}$ ) was added at a flow rate of  $0.50 \text{ mL h}^{-1}$ , followed by 30 min of further stirring. A brownish red solution of AuNRs was then obtained. Centrifugation was carried out to the as-prepared solution at  $8000 \text{ rpm}$  for 40 min (Centrifuge 5810, Eppendorf) to remove the excess of surfactant. The supernatant was discarded and the precipitated AuNRs were collected and resuspended in water to a final volume of  $\approx 20 \text{ mL}$ .

**Modification of Gold Nanorods:** Functional polyethylene glycol (PEG) polymer (HS-PEG-OH,  $M_w = 3000 \text{ Da}$ , Iris Biotech) was dissolved in ethanol (99.8%) to make a  $2.5 \times 10^{-3} \text{ M}$  solution.  $10 \text{ mL}$  of purified AuNRs was diluted to  $100 \text{ mL}$  followed by addition of the ethanolic PEG solution ( $20 \text{ mL}$ ) under stirring. The solution was then sonicated at  $60^\circ\text{C}$  for 30 min and at  $30\text{--}50^\circ\text{C}$  for another  $3.5 \text{ h}$ .<sup>[49]</sup> Stirring of the solution was then carried out overnight. Subsequently, the solution was extracted by chloroform ( $120 \text{ mL}$ , p.a.) for three times to remove the CTAB and unbound PEG. The aqueous phase after extraction was centrifuged for three times, where the supernatant was discarded each time and the precipitate (less than  $2 \text{ mL}$ ) was diluted with dimethyl sulfoxide (DMSO) to  $45 \text{ mL}$ . After the last centrifugation, the residue was collected as a concentrated solution of PEGylated AuNRs in DMSO. UV-vis spectrum (V-630, JASCO) shows that the modified AuNRs have an absorption maximum of longitudinal band at  $791 \text{ nm}$ .<sup>[20]</sup> Analysis based on transmission electron microscope (Zebra 120, Zeiss) reveals that the AuNRs have an average diameter of  $15.4 \text{ nm}$  and length of  $60.0 \text{ nm}$ , i.e., aspect ratio of 3.90.

**Preparation of Nonwetting Template:** Microgel particles were fabricated using nonwetting molds as template. A cleaned microscope slide was placed on top of a diced silicon master ( $2 \text{ cm} \times 2 \text{ cm}$ , for surface structures see Figure S1, Supporting Information) produced

by photolithography (AMO GmbH), where two pieces of four-layered parafilm (Bemis, total thickness  $\approx 400 \mu\text{m}$ ) were used as spacers. Perfluoropolyether-urethane dimethacrylate (PFPE,  $M_w = 2000$ , Fluorolink MD700, Solvay Solexis) containing 1 wt% Darocure 1173 (Ciba Speciality Chemicals) was then injected into the space until it was fully filled. Subsequently, the PFPE was cured for 20 min under a UV lamp ( $366$  and  $254 \text{ nm}$ ,  $4 \text{ W}$  at each wavelength, Konrad Benda) in argon atmosphere. After curing, the PFPE film with replicated structures was carefully peeled off from the silicon master and cut into suitable size ( $6 \text{ mm} \times 6 \text{ mm}$ ). The flat PFPE film was prepared with the same protocol except that another microscope slide was used instead of silicon master.

**Fabrication of AuNR-Laden Microgels:** Cross-linker ( $N,N'$ -methylenebisacrylamide, BIS, 99%) and photoinitiator (2-hydroxy-4'-(2-hydroxyethoxy)-2-methylpropiophenone, 98%) were added at a molar amount of 1% relative to  $N$ -isopropylacrylamide (NIPAM, 97%, recrystallized twice in  $n$ -hexane). A typical monomer solution thus contains NIPAM ( $57.5 \text{ mg}$ ), BIS ( $0.78 \text{ mg}$ ), photoinitiator ( $1.14 \text{ mg}$ ), AuNR solution ( $57.5 \mu\text{L}$ ), and DMSO ( $40.6 \mu\text{L}$ ). The optical density of the solution was  $240$  at  $791 \text{ nm}$  ( $1 \text{ cm}$  optical path) due to the presence of AuNRs.

The fabrication procedure of microgel particles was the same as used in previous reports.<sup>[17,20]</sup> A home-made press with a quartz window was used for the molding of microgel, and all steps were carried out in a glove box ( $\text{O}_2 < 0.2\%$ ). The monomer solution ( $0.5 \mu\text{L}$ ) was first pipetted on the replicated PFPE film, which was then covered by a flat PFPE film. A weight was applied on top of the flat film to generate suitable pressure ( $\approx 260 \text{ kPa}$ ) to the mold. The pressure ensured that only separate elements were formed. The microgels were cured by 20 min of UV irradiation ( $366$  &  $254 \text{ nm}$ , Konrad Benda). Afterward the weight was removed, and the mold was peeled off from the flat film. Bi-layered microgels were produced by sputtering a thin gold film ( $\approx 2 \text{ nm}$ ) on the mold with microgels by a sputter coater ( $30 \text{ mA}$ ,  $20\text{s}$ , Edwards S150B).

To transfer the microgels, microscope slides (Corning glass) were cut into squares ( $25 \text{ mm} \times 25 \text{ mm}$ ) and cleaned with sonication in isopropanol.  $0.5 \text{ mm}$  thick polydimethylsiloxane (PDMS) film (Sylgard 184, Dow Corning) was cut into square frame with outer dimension of  $15 \text{ mm} \times 15 \text{ mm}$  and inner dimension of  $10 \text{ mm} \times 10 \text{ mm}$ . The cleaned glass slide and the PDMS frame were activated in  $\text{O}_2$  plasma ( $200 \text{ W}$ ,  $20 \text{ s}$ ,  $1 \text{ mbar}$ , PVP Tepla 100) and then bound together to form an open chamber. Glycerol (99.5%,  $15 \mu\text{L}$ ) was pipetted in the chamber and the PFPE mold with microgel particles was placed upside down in the chamber. The whole chamber was then stored in a freezer at  $-80^\circ\text{C}$  overnight. Transfer of the microgels was achieved by peeling the PFPE mold off, where the frozen glycerol served as adhesive. The glycerol was subsequently evaporated at  $60^\circ\text{C}$  under vacuum ( $1 \times 10^{-2} \text{ mbar}$ ), leaving only microgels in the PDMS chamber. Deionized water was added to reswell the microgel.

To fabricate the rotor, spiral shaped microgels were mixed with  $10 \mu\text{m}$  nonmodified silica microparticles having hydroxyl terminal groups (DNG-B018, Creative Diagnostics, US). Through stroboscopic irradiation of the microgels with NIR laser ( $0.5\text{--}0.5 \text{ s}$ ) for 5 min, some microspheres were irreversibly adsorbed upon contact with the PNIPAm hydrogel. To minimize bundling of the microgels or the adsorption of several spheres per spiral, the colloidal solution was diluted to  $0.0005 \text{ mg mL}^{-1}$ . In addition, the spirals were fairly separated from each other so that the one that had a microsphere only attached at the end could be found and used. The adhesive strength of the microsphere to hydrogel was apparently sufficient to prevent desorption during the time of the experiment. Indeed, prior confinement, stroboscopic irradiation drove the spiral to translate and rotated sideways, confirming that adhesion of the microsphere to the hydrogel was sufficient to resist drag and friction forces (see Video S1, Supporting Information). The confining gap was fabricated by gluing several round coverslips (diameter:  $10 \text{ mm}$ ) at the center of a  $18 \text{ mm} \times 18 \text{ mm}$  coverslip with epoxy adhesive, which was then used to cover the PDMS chamber containing microgels as illustrated in Figure S2 (Supporting Information). To limit the movement of the microspheres in the XY direction, the microgel was driven by stroboscopic irradiation into the area where the distance between the glass slides approaches  $10 \mu\text{m}$ . As mentioned earlier, photothermal actuation allowed the ribbon to swim freely. This allowed us to move the ribbon gradually from the outside to

the inside center of the confining glass until the silica sphere showed a minor lateral displacement. Apparently, the gap was slightly smaller in the central area (see Video S1, Supporting Information). The confinement was also probed by tracking the XY movement of the sphere. During each actuation cycle, the microsphere undergone a lateral displacement of 2  $\mu\text{m}$  amplitude, but this movement was reversible and confirmed that the microsphere was physically constrained.

**Actuation and Observation of Microgels:** The samples were placed on a Peltier stage mounted on an optical microscope (VHZ-100UR, Keyence). A silicon wafer was placed beneath the sample to enhance optical contrast. The temperature of the Peltier stage was controlled with an accuracy of  $\pm 0.1$  °C. Near infrared (NIR) laser (808 nm, 2.5 W, Roithner Lasertechnik) was focused to the middle of field of view with an incident angle of roughly 40°. The elliptical spot had a diameter of around 1 mm, and the laser intensity in the center of the spot was roughly 1.7 W mm<sup>-2</sup>. The laser was modulated with a temporal resolution of 1 ms. For the spiral rotor, videos were recorded by the microscope camera at a frame rate of 27 frames s<sup>-1</sup>. A short pass filter (700 nm, OD 4, Edmund optics) was inserted between the lens and camera to filter scattered laser. The setup is schematically shown in Figure S3 (Supporting Information).

**Video Analysis:** Acquired videos were analyzed with ImageJ (V1.50c). Superimpositions of the images were done using the *Image Calculator* function. Figure 3b is the superimpositions of thresholded images, to which individual colors were given using *Channel Tools*. To acquire the change in shape of the spiral, the images were inverted, and the contour was fitted by *Ridge Detection* (Figure S4a, Supporting Information). The coordinates of the fitted curve were then exported and analyzed. The length of the center line could be easily calculated by adding up the lengths between adjacent points, while the tangential angle of the free end was measured by linear fitting of the points at the end. In principle, the tangential angle on any point of the centerline could be calculated based on the fitting. As an example, the tangential angle at the half length of the spiral is plotted in Figure S4c (Supporting Information), which shows a qualitatively similar shape as the one in Figure 3d.

## Supporting Information

Supporting Information is available from the Wiley Online Library or from the author.

## Acknowledgements

The authors thank Tamas Haraszti for the help with image analysis. H.Z., A.M., and M.M. acknowledge the funding by DFG-SPP 1726 Microswimmer (Project number: 255087333) and SFB 985 - Functional Microgels and Microgel Systems. This project received funding from the European Research Council (ERC) under the European Union's Horizon 2020 research and innovation program (grant agreement 682754 to E.L.) and ERC - Advanced Grant 695716 to M.M.

## Conflict of Interest

The authors declare no conflict of interest.

## Keywords

microgels, microswimmers, out-of-equilibrium, photothermal actuation, rotational motion, Stokes flow

Received: June 29, 2019

Revised: September 9, 2019

Published online: September 25, 2019

- [1] G. H. Wadhams, J. P. Armitage, *Nat. Rev. Mol. Cell Biol.* **2004**, *5*, 1024.
- [2] E. H. Harris, *Annu. Rev. Plant Physiol. Plant Mol. Biol.* **2001**, *52*, 363.
- [3] H. C. Berg, D. A. Brown, *Nature* **1972**, *239*, 500.
- [4] A. Hamel, C. Fisch, L. Combettes, P. Dupuis-Williams, C. N. Baroud, *Proc. Natl. Acad. Sci. USA* **2011**, *108*, 7290.
- [5] E. M. Purcell, *Am. J. Phys.* **1977**, *45*, 3.
- [6] E. Lauga, T. R. Powers, *Rep. Prog. Phys.* **2009**, *72*, 096601.
- [7] R. Dreyfus, J. Baudry, M. L. Roper, M. Fermigier, H. A. Stone, J. Bibette, *Nature* **2005**, *437*, 862.
- [8] E. Lauga, *Phys. Rev. E* **2007**, *75*, 041916.
- [9] L. Zhu, E. Lauga, L. Brandt, *J. Fluid Mech.* **2013**, *726*, 285.
- [10] J. Elgeti, R. G. Winkler, G. Gompper, *Rep. Prog. Phys.* **2015**, *78*, 056601.
- [11] D. Thomas, D. G. Morgan, D. J. DeRosier, *J. Bacteriol.* **2001**, *183*, 6404.
- [12] B. A. Afzelius, R. Dallai, S. Lanzavecchia, P. L. Bellon, *Tissue Cell* **1995**, *27*, 241.
- [13] C. Brennen, H. Winet, *Annu. Rev. Fluid Mech.* **1977**, *9*, 339.
- [14] E. Lauga, *Annu. Rev. Fluid Mech.* **2016**, *48*, 105.
- [15] W. J. Choi, Y. Jeon, J.-H. Jeong, R. Sood, S. G. Kim, *J. Electroceram.* **2006**, *17*, 543.
- [16] S. Sareh, J. Rossiter, *Smart Mater. Struct.* **2013**, *22*, 014004.
- [17] A. Mourran, H. Zhang, R. Vinokur, M. Möller, *Adv. Mater.* **2017**, *29*, 1604825.
- [18] W. Ni, X. Kou, Z. Yang, J. Wang, *ACS Nano* **2008**, *2*, 677.
- [19] H. H. Richardson, M. T. Carlson, P. J. Tandler, P. Hernandez, A. O. Govorov, *Nano Lett.* **2009**, *9*, 1139.
- [20] H. Zhang, A. Mourran, M. Möller, *Nano Lett.* **2017**, *17*, 2010.
- [21] O. A. Arriagada, G. Massiera, M. Abkarian, *Soft Matter* **2014**, *10*, 3055.
- [22] G. Stoychev, S. Zakharchenko, S. Turcaud, J. W. C. Dunlop, L. Ionov, *ACS Nano* **2012**, *6*, 3925.
- [23] J. Wang, D. Gan, L. A. Lyon, M. A. El-Sayed, *J. Am. Chem. Soc.* **2001**, *123*, 11284.
- [24] C. E. Reese, A. V. Mikhonin, M. Kamenjicki, A. Tikhonov, S. A. Asher, *J. Am. Chem. Soc.* **2004**, *126*, 1493.
- [25] T.-Y. Wu, A. B. Zrimsek, S. V. Bykov, R. S. Jakubek, S. A. Asher, *J. Phys. Chem. B* **2018**, *122*, 3008.
- [26] E. Sato Matsuo, T. Tanaka, *J. Chem. Phys.* **1988**, *89*, 1695.
- [27] T. Ding, V. K. Valev, A. R. Salmon, C. J. Forman, S. K. Smoukov, O. A. Scherman, D. Frenkel, J. J. Baumberg, *Proc. Natl. Acad. Sci. USA* **2016**, *113*, 5503.
- [28] J. Zhao, H. Su, G. E. Vansuch, Z. Liu, K. Salaita, R. B. Dyer, *ACS Nano* **2019**, *13*, 515.
- [29] E. Mabrouk, D. Cuvelier, F. Brochard-Wyart, P. Nassoy, M.-H. Li, *Proc. Natl. Acad. Sci. USA* **2009**, *106*, 7294.
- [30] E. Reyssat, L. Mahadevan, *EPL* **2011**, *93*, 54001.
- [31] P.-G. Gennes, *Scaling Concepts in Polymer Physics*, Cornell University Press, Ithaca, United States **1979**.
- [32] S. J. Gerbode, J. R. Puzey, A. G. McCormick, L. Mahadevan, *Science* **2012**, *337*, 1087.
- [33] H. W. Krenn, *Annu. Rev. Entomol.* **2010**, *55*, 307.
- [34] J. L. Perry, K. P. Herlihy, M. E. Napier, J. M. DeSimone, *Acc. Chem. Res.* **2011**, *44*, 990.
- [35] E. H. Mansfield, *The Bending and Stretching of Plates*, Cambridge University Press, Cambridge **1989**.
- [36] S. Timoshenko, *J. Opt. Soc. Am.* **1925**, *11*, 233.
- [37] S. Schmidt, M. Zeiser, T. Hellweg, C. Duschl, A. Fery, H. Möhwald, *Adv. Funct. Mater.* **2010**, *20*, 3235.
- [38] S. Rose, A. PrevotEAU, P. Elzière, D. Hourdet, A. Marcellan, L. Leibler, *Nature* **2014**, *505*, 382.
- [39] C. Wang, Y. Li, Z. Hu, *Macromolecules* **1997**, *30*, 4727.
- [40] M. Shibayama, T. Tanaka, in *Responsive Gels: Volume Transitions I. Advances in Polymer Science*, Vol 109 (Ed: K. Dušek), Springer, Berlin, Germany **1993**, pp. 1–62.



- [41] S. Palagi, A. G. Mark, S. Y. Reigh, K. Melde, T. Qiu, H. Zeng, C. Parmeggiani, D. Martella, A. Sanchez-Castillo, N. Kapernaum, F. Giesselmann, D. S. Wiersma, E. Lauga, P. Fischer, *Nat. Mater.* **2016**, *15*, 647.
- [42] C. Eloy, E. Lauga, *Phys. Rev. Lett.* **2012**, *109*, 038101.
- [43] R. Chelakkot, A. Gopinath, L. Mahadevan, M. F. Hagan, *J. R. Soc., Interface* **2014**, *11*, 20130884.
- [44] J. Gray, G. J. Hancock, *J. Exp. Biol.* **1955**, *32*, 802.
- [45] A. J. Goldman, R. G. Cox, H. Brenner, *Chem. Eng. Sci.* **1967**, *22*, 637.
- [46] C. Maggi, F. Saglimbeni, M. Dipalo, F. De Angelis, R. Di Leonardo, *Nat. Commun.* **2015**, *6*, 7855.
- [47] G. Vizsnyiczai, G. Frangipane, C. Maggi, F. Saglimbeni, S. Bianchi, R. Di Leonardo, *Nat. Commun.* **2017**, *8*, 15974.
- [48] B. Nikoobakht, M. A. El-Sayed, *Chem. Mater.* **2003**, *15*, 1957.
- [49] M. Bartneck, H. A. Keul, S. Singh, K. Czaja, J. Bornemann, M. Bockstaller, M. Moeller, G. Zwardlo-Klarwasser, J. Groll, *ACS Nano* **2010**, *4*, 3073.